RESEARCH ARTICLE



Journal

Check for updates

Effects of burial powder configuration on the microstructure, composition, and ion conductivity of perovskite $\text{Li}_{3x}\text{La}_{1/3-x}\text{TaO}_3$ ion conductors

Correspondence

Jon F. Ihlefeld, Department of Materials Science and Engineering, University of Virginia, Charlottesville, VA 22904, USA. Email: jihlefeld@virginia.edu

Funding information

J Am Ceram Soc. 2022;1-10.

National Science Foundation's Division of Chemical, Bioengineering, Environmental, and Transport Systems, Grant/Award Number: 2055042

Abstract

A combustion synthesis methodology for the preparation of perovskite $\text{Li}_{3x}\text{La}_{1/3-x}\text{TaO}_3$ lithium-ion conductors with x=0.033 is presented. Bulk ceramic specimens were sintered under combinations of burial powder and cover crucibles to provide different lithium vapor overpressure conditions. A maximum total lithium ion conductivity of 6×10^{-6} S cm⁻¹ at room temperature was found for the pellet covered by a crucible whose lip was sealed using parent powder (moderate overpressure), with agreement to the maximum in the intergranular ion conductivity. Intragranular conductivity was maximized at the low overpressure condition. The trend in ion conductivity was found to correspond to the lithium content in the samples through a combination nuclear reaction analysis and energy dispersive X-ray spectroscopy phase constitution measurements. The mechanism impacting ion conductivity was determined to be changes in the amount of LaTaO_4 secondary phase as driven by the processing conditions during sintering.

KEYWORDS

electrolyte, impedance spectroscopy, ionic conductivity, sinter/sintering

1 | INTRODUCTION

Solid-state, ion conducting ceramics provide a promising avenue for advancing energy storage technology. For lithium ion batteries specifically, solid-state electrolytes offer several potential benefits over liquid electrolytes, including increased energy density and improved safety.¹ Solid-state electrolytes can also offer improved mechanical stability in comparison to liquid electrolyte constructions, conferring enhanced resistance to dendrite formation.^{2,3} In addition, solid-state electrolytes can exhibit electrochemical stability over a broad voltage window, allowing

for construction of batteries with high-energy electrodes as well as reducing the likelihood of a mechanical failure leading to a violent reaction upon exposure to the atmosphere.⁴ Currently, most commercially available solid-state batteries are based on lithium phosphorous oxynitride (LiPON) due to its stability at a wide range of voltages, high lithium ion transference number, and ease of preparation.^{5,6} While LiPON exhibits many of the desirable qualities for a solid-state electrolyte, its ion conductivity is modest (10⁻⁶ S cm⁻¹),⁶ and it is typically only prepared in thin film form. This limits the use of these batteries in high-power applications because they cannot

This is an open access article under the terms of the Creative Commons Attribution-NonCommercial-NoDerivs License, which permits use and distribution in any medium, provided the original work is properly cited, the use is non-commercial and no modifications or adaptations are made.

© 2022 The Authors. Journal of the American Ceramic Society published by Wiley Periodicals LLC on behalf of American Ceramic Society.

¹Department of Materials Science and Engineering, University of Virginia, Charlottesville, Virginia, USA

²Department of Physics, State University of New York at Albany, Albany, New York, USA

³Charles L. Brown Department of Electrical and Computer Engineering, University of Virginia, Charlottesville, Virginia, USA

support the current densities required for fast charging or high-power output, both of which are critical in industries such as the growing electric vehicle segment. Many studies have sought to discover a suitable replacement for LiPON in high-power, solid-state battery applications and while materials have been identified that exceed the ion conductivity of LiPON, many are not yet suitable for deployment in commercial applications due to challenges with processing and integration into battery packages.^{7–10}

Li_{3x}La_{1/3-x}TaO₃ (LLTaO) shares the A-site deficient perovskite structure of the well-known lithium ion conducting system Li_{3x}La_{2/3-x}TiO₃. 11-13 LLTaO exhibits lithium ion conductivity that falls between that of LiPON and the closely related titanate, but due to the valence-stable tantalum ion on the B-site, should not be as susceptible to reactions with high-energy electrodes such as lithium metal and may be better suited for secondary battery applications. 11 However, the LLTaO system has also shown a dependence of conductivity on the lithium content in the system.¹³ Lithium and lithium oxide have high vapor pressures at elevated temperatures, such as those used to sinter polycrystalline ceramic materials. 14 In other systems containing volatile cations, it is common to adjust the sintering atmosphere through the use of burial powder of the same composition to prevent losses of the volatile cation from the ceramic body. 15-21 Specifically in lithium-containing garnets, it has been shown that the powder bed composition can lead to an improvement in the density of the sintered body as well as modifying the ion conductivity. This effect was attributed to changes in the composition of the resulting sintered body due to cations available in the powder bed.²² In this work, a combustion synthesis method for the production of LLTaO powders is presented and the effects of the sintering environment, specifically the burial powder configuration, on the final ceramic body are elucidated. It is shown that the sintering configuration did not have a direct relation to the measured lithium content of the sample, however, minor changes in the lithium content and phase constitution were evident, resulting in changes to the ion conductivity of the samples. Lithium losses during sintering were found to be considerably lower in all samples than predicted based on the vapor pressure of lithium-containing species over lithium oxide, with the overall composition of all samples remaining near the batched composition.

2 | EXPERIMENTAL PROCEDURES

Polycrystalline, bulk ceramic samples of $\text{Li}_{3x}\text{La}_{1/3-x}\text{TaO}_3$, where x = 0.033, were prepared by a combustion synthesis approach. Solutions of 0.4 M LiNO₃ (99.999%, Alfa Aesar) in ethanol and 1.9 M lanthanum acetate (99.9%, Alfa

Aesar) in propionic acid were prepared from powder precursors. Ta₂O₅ powder (99.9%, H.C. Starck) was suspended in ethanol by stirring at room temperature; during mixing, a stoichiometric amount of the lanthanum-containing solution and a 20 at.% excess of the lithium-containing solution were added to the Ta₂O₅ suspension. The precursors were allowed to mix at room temperature overnight. Ethanol was then driven out of the solution by continuing to mix on a hotplate set at 80°C. The solution was dried further at 130°C in a drying oven. The resulting mass was ground using a mortar and pestle before calcining at 1050°C for 8 h. Calcined powders were ground in a mortar and pestle before being uniaxially pressed at 175 MPa in a 12.7 mm diameter die without binder to form pellets with a green mass of approximately 1.7 g. Resultant pellets had green densities between 49% and 50% of the theoretical value. Pellets were then loaded into the furnace for sintering according to the diagrams shown in Figure 1, where the burial powder configuration was altered in an effort to provide varying levels of lithium overpressure within the sintering vessel. Five sintering configurations were used in this study: the "none overpressure condition" consisting of the pellet set directly on the setter with no aids to lithium vapor pressure as shown in Figure 1A; the "low overpressure condition," where the pellet was placed under a cover crucible with no burial powder, as shown in Figure 1B; the "moderate overpressure condition," where the pellet was placed under a cover crucible that was sealed by a ring of burial powder (note that there is no contact between the pellet and burial powder) as shown in Figure 1C; the "high overpressure condition," which used a cover crucible configured as in the moderate condition, but with an additional pile of burial powder adjacent to the pellet, as shown in Figure 1D; and the "very high overpressure condition," which used a cover crucible as in the moderate condition, but with the pellet buried within a mound of burial powder, as shown in Figure 1E. All burial powder used was of the same nominal composition as the pellets, including lithium excesses. Additionally, the amount of burial powder used for the sealing rings in all configurations was measured to be within 5% by mass for each condition. The high and very high overpressure conditions used the same amount of additional powder within the crucible. All samples were sintered at 1500°C for 12 h in a box furnace in a static air atmosphere. Density of the sintered samples was measured geometrically. The circular faces of the pellet were ground to create flat surfaces onto which 50 nm thick palladium electrodes were sputtered. X-ray diffraction (XRD) patterns were collected using a Panalytical Empyrean diffractometer, using Cu-Kα radiation in Bragg-Brentano geometry with a GaliPIX detector in scanning line mode (Malvern Panalytical, Malvern, UK). Impedance spectra were measured between 2 MHz

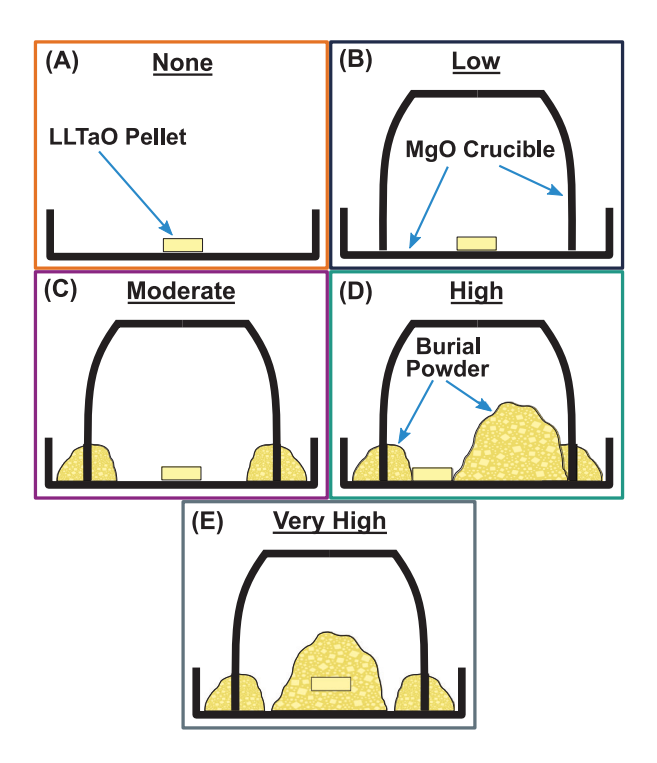


FIGURE 1 Diagram of the differing sintering conditions. The boxes outlining each condition diagram serve as a key to the colors used to represent data for each condition throughout the manuscript. (A) The none overpressure condition consisting of the pellet set directly on the setter with no aids to lithium vapor pressure. (B) The low overpressure condition, where the pellet was placed under a cover crucible with no burial powder. (C) The moderate overpressure condition, where the pellet was placed under a cover crucible that was sealed by a ring of burial powder (note that there is no contact between the pellet and burial powder). (D) The high overpressure condition, which used a cover crucible configured as in the moderate condition, but with an additional pile of burial powder adjacent to the pellet. (E) The very high overpressure condition which used a cover crucible as in the moderate condition, but with the pellet buried within a mound of burial powder.

and 20 Hz with an oscillator of 500 mV using an Agilent E4980A LCR meter (Agilent, Santa Clara, CA, USA). A Sun EC1A environmental chamber (Sun Electronic Systems, Titusville, FL, USA) and a custom pellet test fixture were used to perform measurements between 25°C and 300°C. Complex plane impedance spectra were fit using EC-Lab fitting software (Bio-Logic S.A.S., Claix, France) for calculation of conductivity values. Activation energies were calculated using an Arrhenius-type analysis for an activated process. ^{24,25} Plan view scanning electron microscopy (SEM) was performed using an FEI Quanta 650 scanning electron microscope (Thermo Fisher Scientific, Waltham, MA, USA) with accelerating voltage of 20 kV in backscatter imaging mode. Grain size measurements were performed using the Hilliard method from ASTM E112.²⁶ Energy dispersive X-ray spectroscopy (EDS) composition maps were

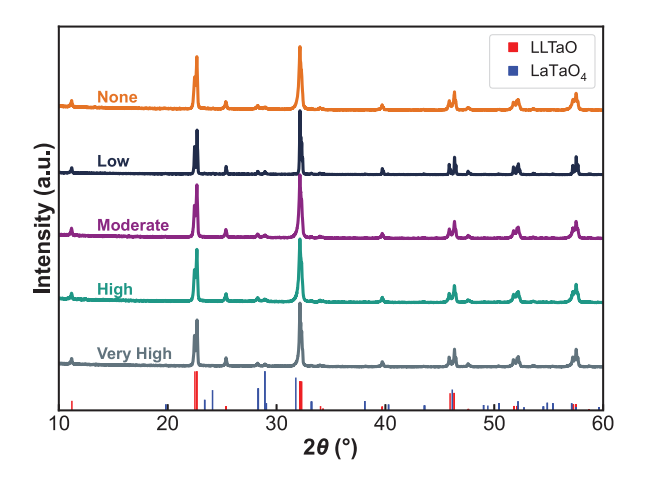


FIGURE 2 Comparison of X-ray diffraction (XRD) patterns for each sintering condition. Sintering condition is noted in color-matched font above each pattern. Bar markers along the abscissa indicate peak positions and relative intensities for of reference patterns of for the A-site deficient perovskite with x = 0 LLTaO (ICSD Collection Code 20281)²⁸ and orthorhombic LaTaO₄ (ICSD Collection Code 238801).²⁹

captured on a Thermo Fisher Scientific Phenom XLG2 scanning electron microscope (Thermo Fisher Scientific) system with an accelerating voltage of 20 kV and phase fraction analyses were performed following the methods in ASTM E562. Lithium content was determined by nuclear reaction analysis (NRA) performed at the State University of New York at Albany ion beam line, using the $7\text{Li}(p,\alpha)\alpha$ nuclear reaction. Samples were irradiated with 50 μ C of 1.2 MeV protons, resulting in alpha particles that were detected on a Si detector at 168° to the beamline. Quantified lithium to tantalum ratios were determined using a SAW-grade Li_{0.946}TaO_{2.97} single crystal (MTI Corporation) as a standard.

3 | RESULTS AND DISCUSSION

Figure 2 shows the XRD patterns of each pellet after sintering under their respective overpressure conditions. Reference patterns are shown as red and blue bar markers along the abscissa for the A-site deficient perovskite with x = 0 (ICSD Collection Code 20281)²⁸ and orthorhombic LaTaO₄ secondary phase (ICSD Collection Code 238801),²⁹ respectively. The majority of peaks in the pattern are well matched with the tetragonal phase of LLTaO, reported to exist below a lithium content of x = 0.075 by Mizumoto and Hayashi.³⁰ The tetragonal LLTaO phase is made up of a supercell of two pseudocubic perovskite cells that exhibit ordering of the lanthanum atoms on alternating (100) planes. Two impurity phase peaks are present between 25° and 30° in 2 θ that are well indexed to the high-intensity

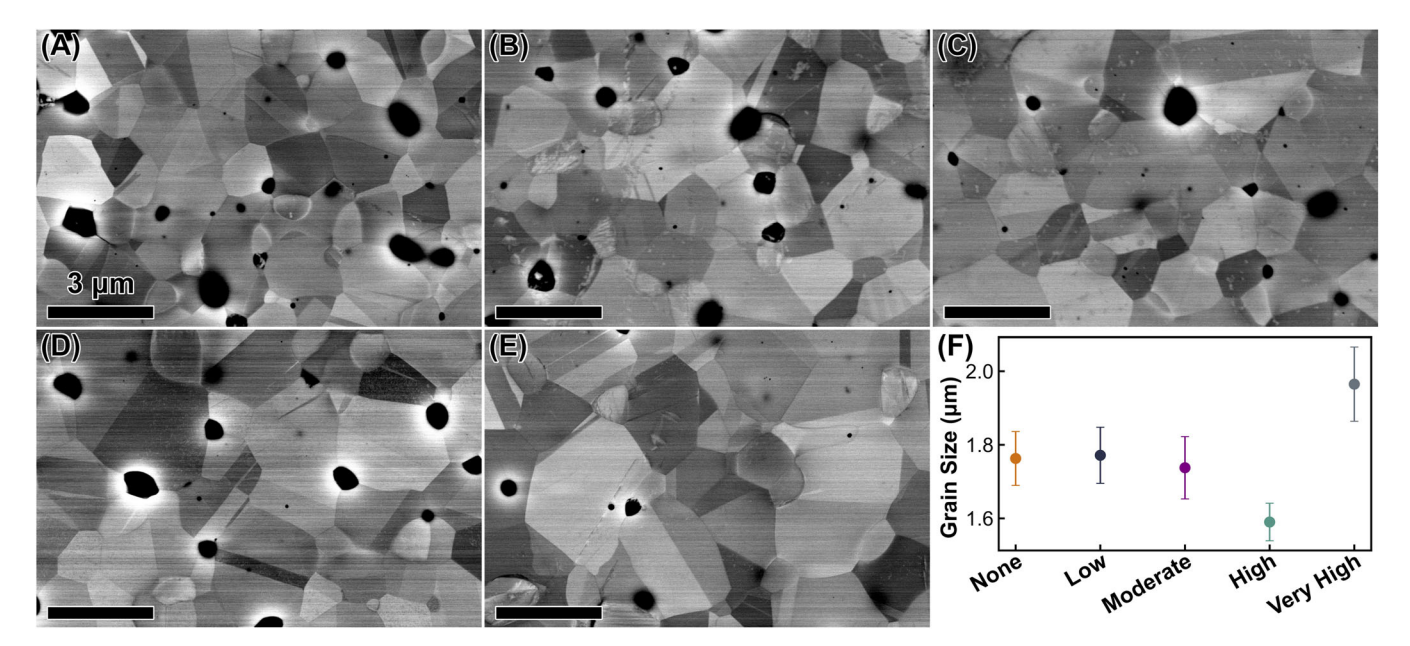


FIGURE 3 Representative backscatter scanning electron micrographs taken from polished cross-sections of the (A) none, (B) low, (C) moderate, (D) high, and (E) very high overpressure condition pellets. (F) Plot of the measured average grain size as a function of sintering overpressure condition. Error bars indicate 95% confidence intervals.

peaks of the orthorhombic LaTaO₄ phase. The magnitude of the reference pattern bar markers serves to indicate the expected relative intensity of each reflection. Comparison to the observed patterns reveals no preferred texture in the samples. Notably, the LLTaO peak at 32° in 2θ appears to be of greater intensity than expected, but this is due to the superposition of the (110) and (102) peaks within the resolution of the diffractometer. Comparison between the patterns of differing sintering conditions reveals no major changes in crystal structure or texture. Furthermore, the ratio of the LLTaO (100) and (001) peak intensities are approximately constant, indicating that the level of A-site ordering is not changing with sintering condition. Similarly, a comparison of the relative intensities for LaTaO₄ to the LLTaO shows a constant ratio, within sensitivity limits, for all sintering conditions.

Cross-sectional scanning electron backscatter micrographs of pellets derived from each overpressure condition are shown in Figure 3A–E. Contrast in these micrographs derives from electron channeling effects and differential backscatter yields of different crystal orientations in the material. The micrographs shown in Figure 3 are provided at a higher magnification than those used in characterization efforts. Representative micrographs at the magnification used in characterization are provided in Figure S1. In all samples, there are apparent voids throughout the material, which appear to be residual porosity. Porosity was calculated from the micrographs by thresholding the void areas, resulting in values ranging from 2% to 4% by area. This value is consistent with geometrically derived density

of the pellets, after accounting for error in the geometric measurement and potential implicit bias toward imaging areas with less porosity. Geometric density values ranged from 93% to 95% of the theoretical value with no clear trend with sintering condition. In all samples, there are visible twins in some grains, which is consistent with the observation of tetragonal ordering peaks observed in the XRD patterns. Qualitative examination of the SEM micrographs shows that most grains are equiaxed. The microstructure also appears to have a bimodal or multimodal grain size distribution; however, this was not quantitatively studied. Average grain size was found to be 1.76 \pm 0.07 μ m, $1.77 \pm 0.08 \ \mu \text{m}, \ 1.73 \pm 0.08 \ \mu \text{m}, \ 1.59 \pm 0.05 \ \mu \text{m}, \ \text{and}$ $1.96 \pm 0.10 \,\mu m$ for the none, low, moderate, high, and very high overpressure conditions, respectively. These values are plotted against the sintering condition in Figure 3F, where the error bars represent the 95% confidence interval for the measurements. The average grain size is nearly constant for the three lowest overpressure sintering conditions. While the high and very high overpressure conditions do fall slightly outside the 95% confidence interval of the other points, they do not form a trend that corresponds directly with the sintering condition or with the ion conductivity results shown in Figure 4.

Ion conductivity was determined using impedance spectroscopy (IS), which measures frequency-dependent response of a material under alternating current fields. Figure 4A shows representative complex plane impedance spectra from each overpressure condition at 25°C. Each spectrum is composed of two leading arcs followed by

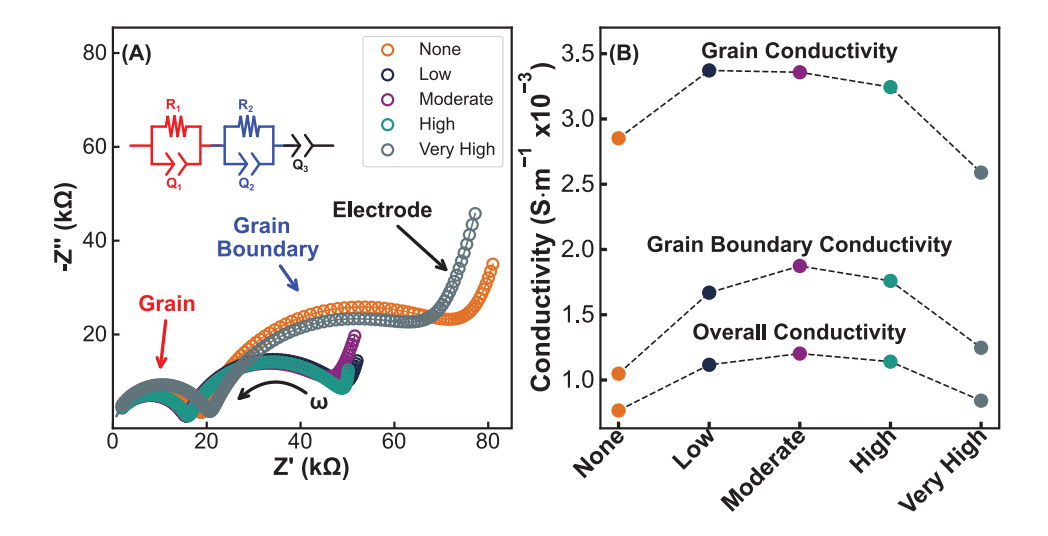


FIGURE 4 (A) Room temperature complex plane impedance spectra for each overpressure condition. Experimental data (without geometric correction) is represented as open points with the fit plotted as a line of the same color. The equivalent circuit used for fitting is illustrated in the upper left of the panel and is color coded to indicate which part of the spectra is represented by each element. (B) Extracted room temperature ion conductivity values from the impedance spectra, separated by the microstructural feature leading to the response.

a final spike. Impedance data were then fit using the equivalent circuit illustrated in Figure 4A, where a ZARC element (resistor in parallel with a constant phase element) is used to model each of the arcs that appear in the spectrum and a final constant phase element represents the blocking palladium electrode spike. The resulting fits are plotted as solid lines of the same color as the experimental data, and good agreement of the fit to the measured data is achieved. Because the grain and grain boundary responses are clearly separable in the impedance spectra, each response can be treated individually. Using the fitted values for the resistor and constant phase elements, an ideal capacitance value can be calculated for each response using the equation for the time constant, $\tau_i = (R_i Q_i)^{1/a} = R_i C_i$, where τ_i is the time constant for the ZARC i, R_i is the resistance of the ZARC, Q_i is the constant phase element value, a is the constant phase element exponent, and C_i is the ideal capacitance to be extracted.³¹ Comparison of the resulting capacitance reveals that R_1 is associated with the grain response, while R_2 is associated with the grain boundary response.³² Then, the grain resistance is R_1 , the grain boundary resistance is R_2 , and the total resistance is $R_1 + R_2$. The ion conductivity was calculated by $\sigma_i = L/(R_i \times A)$, where σ_i is the conductivity of the response associated with ZARC i, L is the perpendicular length between the electrodes, A is the area of the electrodes, and R_i is the fitted resistance for ZARC *i*. The results of this calculation are shown in Figure 4B, with Table S1 showing the fitted values and error for each spectrum at room temperature. Examination of the ion conductivity trend reveals a maximum in the overall ion conductivity at the moderate overpressure condition, corresponding to the

maximum conductivity in the grain boundary response. However, the grain response shows a maximum under the low overpressure condition indicating that the grain boundary response dominates the overall ion conductivity, as can be expected based on prior observations.^{33–35}

Activation energy was determined by measuring the impedance response at temperatures ranging from 25°C to 300°C. An example of the impedance spectra measured from the moderate overpressure sample at several different temperatures is shown in Figure 5A. An Arrhenius plot of the resulting temperature-dependent ion conductivity for the moderate overpressure sample is shown in Figure 5B for each of the grain, grain boundary, and overall responses. Temperature-dependent impedance spectra and Arrhenius plots for activation energy are shown for the other overpressure conditions in Figures S2–S5. The Arrhenius-type relation used is shown below:

$$\sigma T = \sigma_0 e^{-E_a/kT} \rightarrow \ln(\sigma T) = -\frac{E_a}{k} \times \frac{1}{T} + \ln(\sigma_0)$$

where σ is the ion conductivity, T is the absolute measurement temperature, σ_0 is a prefactor, E_a is the activation energy, and k is the Boltzmann constant. Fitting the ion conductivities versus inverse temperature enables calculation of the activation energies of lithium ion conduction. A summary of the activation energies for each sample is shown as a function of sintering overpressure in Figure 5C. It is observed that the grain boundary conduction activation energy is the highest, followed by the overall and grain responses. These results match well with previous literature as well as theoretical predictions on the

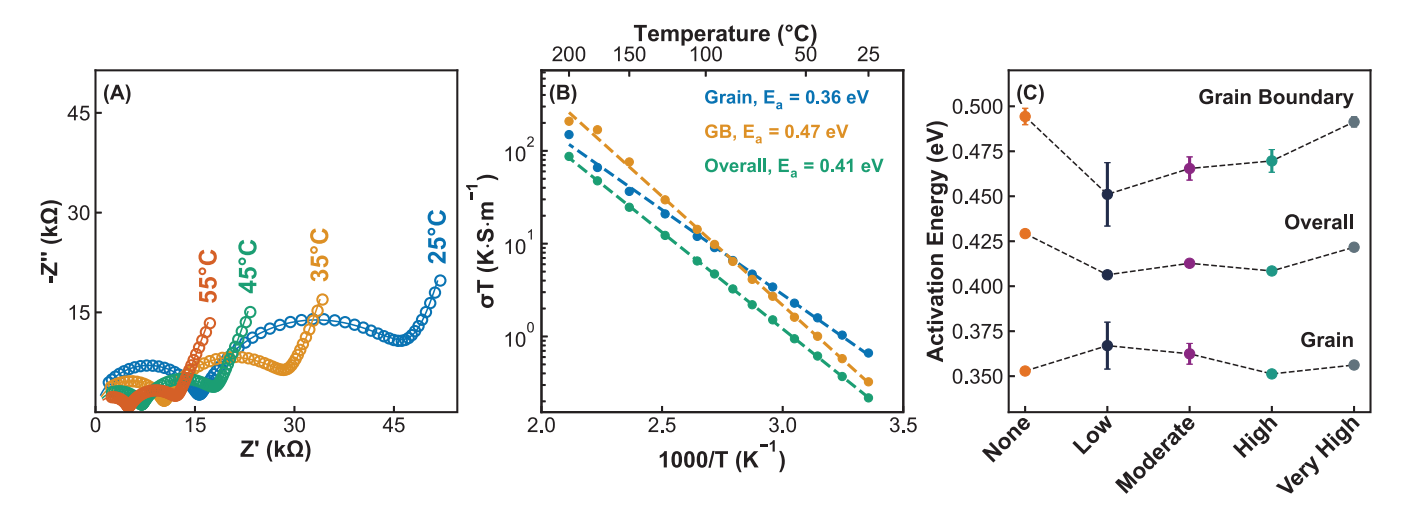


FIGURE 5 (A) Representative impedance spectra from the moderate overpressure sample at temperatures ranging from 25°C to 55°C. (B) Arrhenius plot of the dependence of lithium ion conductivity on temperature for the moderate overpressure sample. Activation energy for individual responses was extracted from the linear fit to the data and noted in the upper right of the plot. (C) Summary of the activation energy values measured for each overpressure condition. Error bars depict the 95% confidence interval for each data point and are present for all data points, but are smaller than the marker in some cases.

mechanisms of lithium ion conductivity, where the grain boundary is resistive due to one of several effects, the grain response is facile due to the high crystallinity and many equivalent sites in the A-site defective perovskite lattice, and finally, the overall response represents some value intermediate to the other responses because it is a combination of both responses over the volume of the sample. 11,33,36 Further comparison of these results to the ion conductivity trends that were observed at room temperature does not reveal a clear correlation between the activation energy and the ion conduction in these samples, indicating that the local environment for lithium ion conduction is similar between all samples.

To further investigate the origin of the change in ion conductivity with sintering condition of LLTaO, NRA was performed on each sample to quantitatively measure the lithium to tantalum ratio. NRA quantifies the abundance of each element by measuring the byproducts of the interaction of high-energy particles with the nuclei of the atoms in the test material. In the case of lithium, the reaction employed takes the form shown in the following equation:

$$_{3}^{7}\text{Li} + _{1}^{1}p \Rightarrow _{2}^{4}\alpha + _{2}^{4}\alpha$$

By measuring the number of alpha particles (α) that are produced by a known proton (p) flux, lithium nuclei can be counted indirectly. The results of the NRA analysis are shown in Figure 6, where the lithium to tantalum ratio is plotted against the sintering overpressure condition. The values determined for each sample follow a trend inverted from the overall ion conductivity; however, the scale of

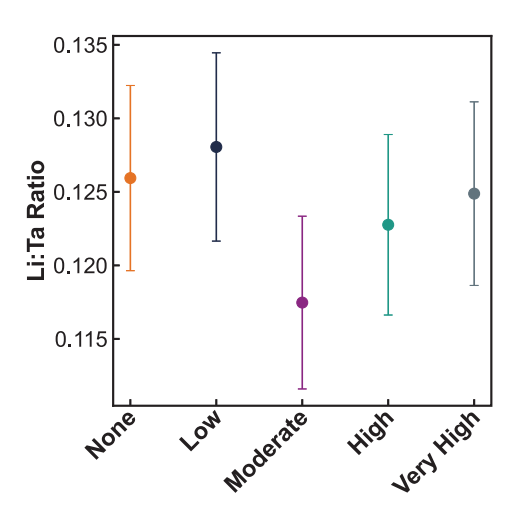


FIGURE 6 Lithium to tantalum ratios determined by nuclear reaction analysis. Error bars represent the statistical counting error calculated for each sample and are approximately equal to 5% for all samples.

the error bars on these values prevent drawing meaningful conclusions from the NRA data alone. Of note, the Li:Ta ratio in all samples is arrayed around 0.12, which is the original batch ratio of Li:Ta when including the lithium excess. This indicates that the vapor phase losses of lithium during sintering are significantly lower than expected based on the vapor pressure of lithium-containing species over lithium oxide. The apparent low lithium vapor pressure over LLTaO could also explain the small variation in sample composition with changes in sintering condition. Assuming that lithium only resides in the

perovskite phase, which is reasonable given that no lithium-containing secondary phases were observed, the lithium to tantalum ratio measured implies an increase in the value of x. Increasing the value of x indicates that less lanthanum can exist in the perovskite phase to satisfy electroneutrality, which leads to the conclusion that the batched composition effectively has an excess of lanthanum. This is consistent with the identification of $LaTaO_4$ in the XRD patterns shown in Figure 1, because a lanthanum-rich phase would need to form to accommodate its excess.

Studies of the closely related lithium lanthanum titanate have reported secondary phases and compositional deviation at the grain boundary, including Li2CO3 and a Ti-O layer that was observed via transmission electron microscopy studies.^{34,37} However, the appearance of the LaTaO₄ secondary phase in XRD indicates that the excess lithium in the samples in this study is being accommodated within the LLTaO lattice, resulting in expelling other cations to maintain charge balance and due to the valence stability of tantalum, the reduction mechanism that is observed in the titanate is unlikely to occur in these samples. To investigate the location and prevalence of the secondary phase, EDS was performed on the same samples that were used for grain size measurements. The lanthanum and tantalum signals were superimposed to create maps that represent LaTaO₄, where the lanthanum concentration is enhanced and LLTaO, where the tantalum concentration is high. Representative, combined EDS maps from each sintering condition are shown in Figure S6. Comparison of the EDS maps with backscatter imaging of the same region did not indicate that LaTaO₄ grains were differently sized from LLTaO grains and that the secondary phase was not obviously delineated by intensity contrast in backscatter imaging mode. Backscatter electron images are shown in Figure S7 for the same fields that are represented as EDS maps in Figure S6. This suggests that the LaTaO₄ phase is present as discrete, discontinuous grains within the microstructure. The procedures from ASTM E562 were then applied to these maps in order to determine the volumetric phase fraction of LaTaO₄ in the samples. The results of this phase fraction analysis are shown in Figure 7. This plot illustrates a bowl-like trend that aligns well with the lithium to tantalum ratios that were found in Figure 6, and matches well with the trend of the overall ion conductivity found in Figure 4, when inverted. These data points are much better differentiated than the Li:Ta ratios, which lends confidence to the absolute values of the lithium content measured by NRA because, as discussed above, larger amounts of the LaTaO4 secondary phase can be expected for larger excesses of lithium. Finally, the phase fraction analysis indicates that the samples contain between 12% and 16% LaTaO₄, which appears to be more

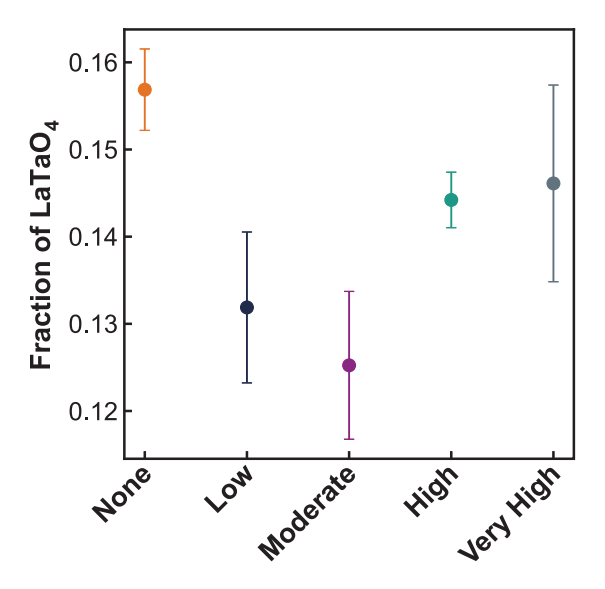


FIGURE 7 Phase fraction of LaTaO $_4$ as a function of the sintering overpressure condition as determined from cross-sectional energy dispersive X-ray spectroscopy (EDS) maps. Error bars represent the 95% confidence interval from the analysis.

than that observed in XRD based on the peak intensity ratios (Figure 2). There are several potential explanations for this discrepancy: (1) The X-ray beam used in diffraction has a penetration depth of between 3.8 and 4.4 μ m^{38,39} on the exterior surface of the pellet, the most likely region of depleted lithium in the samples. Spatially resolved lithium quantification was not possible through NRA, so it is possible that a layer of reduced lithium content is formed on the exterior of the pellet, reducing the phase fraction of LaTaO₄ in that volume and resulting in the relatively low level of XRD intensity for the secondary phase. (2) The analysis of phase fraction makes an assumption that the micrographs represent a 2D slice of the material; however, the electron interaction volume in LLTaO at 20 kV and the large dose used for EDS extend 1.8 µm into the sample, as calculated using a Monte-Carlo simulation from the NIST DTSA-II software package. 40,41 This is approximately the average diameter of a grain; however, most grains on a polished surface are partially removed and will not extend their full diameter into the plane of the image. This indicates that the EDS maps may represent a thicker slice of the material than assumed, leading to overcounting of the presence of LaTaO₄ in the material. (3) A final option, although unlikely based on the thermal budget of these samples, is that the LaTaO₄ within the sample is not fully crystallized leading to reduced signal in the XRD patterns. In total, this suggests that the changing ion conductivity in LLTaO with sintering configuration is primarily driven by the minor changes in amount of lithium vapor evolution during the high-temperature sintering step. The change in lithium concentration then drives the formation

of LaTaO₄ secondary phase particles that act as a resistive element in the material, reducing the overall ion conductivity. Specifically, the secondary LaTaO₄ phase is unlikely to be capable of transporting lithium, therefore, a lithium ion approaching the boundary between a LLTaO and a LaTaO₄ grain would need to be transported around the LaTaO₄ grain through the resistive boundary. Conversely, in the case where a lithium ion encounters a LLTaO-LLTaO grain boundary, it would be transported into the next grain, across the grain boundary. This would manifest in the IS spectra as an increase in the impedance of the grain boundary response. This also explains the relatively constant activation energy of the samples because the conditions for lithium ion conduction in the LLTaO lattice are not changing significantly from sample to sample. This would indicate that the composition within the LLTaO grains in the samples is similar for all overpressure conditions, as the composition of LLTaO can have a strong effect on the ion conductivity that is observed. 13 A recent work on Li_{0.33}La_{0.56}TiO₃ has shown a similar effect wherein the composition of the major phase was constant with changing amounts of secondary phase, indicating a change in overall composition.⁴²

4 | CONCLUSIONS

In summary, it has been shown that minor variations in the lithium concentration in LLTaO can lead to minor changes in the ion conductivity. The mechanism for this appears to be the changes in lithium content leading to increased formation of a secondary phase that hinders the overall lithium ion conduction response by effectively increasing the length of grain boundary through which a lithium ion must transport. This is supported by the grain boundary response acting as the dominant contribution to the total ion conductivity, as well as its inverse correlation with the Li:Ta ratio and the phase fraction of LaTaO₄. Further, these data indicate that the high vapor pressure of lithium that is known to exist for lithium metal and its oxides does not strongly affect LLTaO, as shown by the lithium to tantalum ratios, determined by NRA, remaining very near the batching composition including excess that was added to accommodate predicted lithium losses. It is likely that the apparent low vapor pressure of lithium over LLTaO also contributed to the observation of only small changes in lithium concentration with sintering condition. Conversely, it is unclear how variations in the sintering configuration affected the lithium content in each sample, implying that control over the lithium content would need to be studied further and is likely furnace and sintering environment specific. Finally, the activation energy appears to have a weak dependence on the lithium

content, as it remains constant with minor variations in the Li:Ta ratio. It is proposed that this is due to the local lithium environment in the bulk and grain boundaries remaining nearly constant due to compensation through the formation of a secondary phase.

ACKNOWLEDGMENTS

The authors acknowledge the National Science Foundation's Division of Chemical, Bioengineering, Environmental, and Transport Systems (CBET) for their funding of this work under award number 2055042. Any opinions, findings, and conclusions or recommendations expressed in this manuscript are those of the authors and do not necessarily reflect those of the National Science Foundation.

ORCID

Ian A. Brummel https://orcid.org/0000-0002-3287-6686 *Jon F. Ihlefeld* https://orcid.org/0000-0003-0166-8136

REFERENCES

- Kim JG, Son B, Mukherjee S, Schuppert N, Bates A, Kwon O, et al. A review of lithium and non-lithium based solid state batteries. J Power Sources. 2015;282:299–322. https://doi.org/10. 1016/j.jpowsour.2015.02.054
- Herbert EG, Tenhaeff WE, Dudney NJ, Pharr GM. Mechanical characterization of LiPON films using nanoindentation. Thin Solid Films. 2011;520(1):413–8. https://doi.org/10.1016/j.tsf.2011. 07.068
- Deng T, Ji X, Zhao Y, Cao L, Li S, Hwang S, et al. Tuning the anode–electrolyte interface chemistry for garnet-based solid-state Li metal batteries. Adv Mater. 2020;32(23):2000030. https://doi.org/10.1002/adma.202000030
- Zheng F, Kotobuki M, Song S, Lai MO, Lu L. Review on solid electrolytes for all-solid-state lithium-ion batteries. J Power Sources. 2018;389:198–213. https://doi.org/10.1016/j. jpowsour.2018.04.022
- Hamon Y, Douard A, Sabary F, Marcel C, Vinatier P, Pecquenard B, et al. Influence of sputtering conditions on ionic conductivity of LiPON thin films. Solid State Ion. 2006;177(3):257-61. https://doi.org/10.1016/j.ssi.2005.10.021
- Yu X, Bates JB, Jellison GE Jr., Hart FX. A stable thin-film lithium electrolyte: lithium phosphorus oxynitride. J Electrochem Soc. 1997;144(2):524. https://doi.org/10.1149/1.1837443
- Gao Z, Sun H, Fu L, Ye F, Zhang Y, Luo W, et al. Promises, challenges, and recent progress of inorganic solidstate electrolytes for all-solid-state lithium batteries. Adv Mater. 2018;30(17):1705702. https://doi.org/10.1002/adma.201705702
- Famprikis T, Canepa P, Dawson JA, Islam MS, Masquelier C. Fundamentals of inorganic solid-state electrolytes for batteries. Nat Mater. 2019;18(12):1278–91. https://doi.org/10.1038/s41563-019-0431-3
- 9. Miao X, Wang H, Sun R, Wang C, Zhang Z, Li Z, et al. Interface engineering of inorganic solid-state electrolytes for high-performance lithium metal batteries. Energy Environ Sci. 2020;13(11):3780–822. https://doi.org/10.1039/D0EE01435D
- Yu T, Yang X, Yang R, Bai X, Xu G, Zhao S, et al. Progress and perspectives on typical inorganic solid-state electrolytes. J Alloys

- Compd. 2021;885:161013. https://doi.org/10.1016/j.jallcom.2021.
- Inaguma Y, Liquan C, Itoh M, Nakamura T, Uchida T, Ikuta H, et al. High ionic conductivity in lithium lanthanum titanate.
 Solid State Commun. 1993;86(10):689–93. https://doi.org/10. 1016/0038-1098(93)90841-A
- 12. Mizumoto K, Hayashi S. Lithium ion conduction in A-site deficient perovskites $R_{1/4}Li_{1/4}TaO_3$ (R = La, Nd, Sm and Y). Solid State Ion. 1999;116(3):263–9. https://doi.org/10.1016/S0167-2738(98)00414-7
- Mizumoto K, Hayashi S. Lithium ion mobility and activation energy for lithium ion conduction in A-site deficient perovskites La_{1/3-x}Li_{3x}TaO₃. J Ceram Soc Jpn. 1998;106(1232):369–71. https://doi.org/10.2109/jcersj.106.369
- 14. Lamoreaux RH, Hildenbrand DL. High temperature vaporization behavior of oxides. I. Alkali metal binary oxides. J Phys Chem Ref Data. 1984;13(1):151–73. https://doi.org/10.1063/1.555706
- Dih JJ, Fulrath RM. Electrical conductivity in lead zirconatetitanate ceramics. J Am Ceram Soc. 1978;61(9–10):448–51. https://doi.org/10.1111/j.1151-2916.1978.tb09357.x
- 16. Wang H-C, Schulze WA. The role of excess magnesium oxide or lead oxide in determining the microstructure and properties of lead magnesium niobate. J Am Ceram Soc. 1990;73(4):825–32. https://doi.org/10.1111/j.1151-2916.1990.tb05121.x
- 17. Hu Z, Sheng J, Chen J, Sheng G, Li Y, Fu X-Z, et al. Enhanced Li ion conductivity in Ge-doped Li 0.33 La 0.56 TiO 3 perovskite solid electrolytes for all-solid-state Li-ion batteries. New J Chem. 2018;42(11):9074–9. https://doi.org/10.1039/C8NJ01113C
- 18. Kwon WJ, Kim H, Jung K-N, Cho W, Kim SH, Lee J-W, et al. Enhanced Li + conduction in perovskite Li_{3x}La_{2/3-x}□_{1/3-2x}TiO₃ solid-electrolytes via microstructural engineering. J Mater Chem A. 2017;5(13):6257–62. https://doi.org/10.1039/C7TA00196G
- Wang Y, Lai W. High ionic conductivity lithium garnet oxides of Li_{7-x}La₃Zr_{2-x}Ta_xO₁₂ compositions. Electrochem Solid-State Lett. 2012;15(5):A68. https://doi.org/10.1149/2.024205esl
- Ramakumar S, Janani N, Murugan R. Influence of lithium concentration on the structure and Li+ transport properties of cubic phase lithium garnets. Dalton Trans. 2014;44(2):539–52. https:// doi.org/10.1039/C4DT02861A
- 21. Nemori H, Matsuda Y, Mitsuoka S, Matsui M, Yamamoto O, Takeda Y, et al. Stability of garnet-type solid electrolyte $\text{Li}_x \text{La}_3 \text{A}_{2-y} \text{B}_y \text{O}_{12}$ (A = Nb or Ta, B = Sc or Zr). Solid State Ion. 2015;282:7–12. https://doi.org/10.1016/j.ssi.2015.09.015
- Lobe S, Bauer A, Sebold D, Wettengl N, Fattakhova-Rohlfing D, Uhlenbruck S. Sintering of Li-garnets: impact of Alincorporation and powder-bed composition on microstructure and ionic conductivity. Open Ceram. 2022;10:100268. https:// doi.org/10.1016/j.oceram.2022.100268
- Brown-Shaklee HJ, Ihlefeld J, Spoerke ED, Blea-Kirby MA. Method for producing dense lithium lanthanum tantalate lithium-ion conducting ceramics. US Patent 9963394B2. 2018.
- 24. Kingery WD, Bowen HK, Uhlmann DR. Introduction to ceramics. 2nd ed. New York: Wiley; 1976.
- 25. Nuernberg RB. Numerical comparison of usual Arrhenius-type equations for modeling ionic transport in solids. Ionics. 2020;26(5):2405–12. https://doi.org/10.1007/s11581-019-03243-7

- 26. ASTM E112-13. Test methods for determining average grain size. ASTM International; 2013. https://doi.org/10.1520/E0112-13
- ASTM E562-19. Test method for determining volume fraction by systematic manual point count. ASTM International; 2019. https://doi.org/10.1520/E0562-19E01
- 28. Trunov V, Lykova L, Afonskii N. The structure of Y_{0.33}TaO₃ and La_{0.33}TaO₃. Vestn Mosk Univ Seriya 2 Khimiya. 1968;9(1):55–8.
- Cordrey KJ, Stanczyk M, Dixon CAL, Knight KS, Gardner J, Morrison FD, et al. Structural and dielectric studies of the phase behaviour of the topological ferroelectric La_{1-x}Nd_xTaO₄. Dalton Trans. 2015;44(23):10673–80. https://doi.org/10.1039/ C4DT03721A
- Mizumoto K, Hayashi S. Crystal structure and lithium ion conductivity of A-site deficient perovskites La_{1/3-x}Li₃xTaO₃. J Ceram Soc Jpn. 1997;105(1224):713–5. https://doi.org/10.2109/jcersj.105.
- 31. Guo X, Sigle W, Maier J. Blocking grain boundaries in yttriadoped and undoped ceria ceramics of high purity. J Am Ceram Soc. 2003;86(1):77–87. https://doi.org/10.1111/j.1151-2916. 2003.tb03281.x
- Irvine JTS, Sinclair DC, West AR. Electroceramics: characterization by impedance spectroscopy. Adv Mater. 1990;2(3):132–8. https://doi.org/10.1002/adma.19900020304
- Denk I, Claus J, Maier J. Electrochemical investigations of SrTiO₃ boundaries. J Electrochem Soc. 1997;144(10):3526–36. https://doi.org/10.1149/1.1838044
- Sasano S, Ishikawa R, Sánchez-Santolino G, Ohta H, Shibata N, Ikuhara Y. Atomistic origin of Li-ion conductivity reduction at (Li_{3x}La_{2/3-x})TiO₃ grain boundary. Nano Lett. 2021;21(14):6282–8. https://doi.org/10.1021/acs.nanolett.1c02174
- Sasano S, Ishikawa R, Kawahara K, Kimura T, Ikuhara YH, Shibata N, et al. Grain boundary Li-ion conductivity in (Li_{0.33}La_{0.56})TiO₃ polycrystal. Appl Phys Lett. 2020;116(4):043901. https://doi.org/10.1063/1.5141396
- 36. Li R, Liao K, Zhou W, Li X, Meng D, Cai R, et al. Realizing four-fold enhancement in conductivity of perovskite Li_{0.33}La_{0.557}TiO₃ electrolyte membrane via a Sr and Ta co-doping strategy. J Membr Sci. 2019;582:194–202. https://doi.org/10.1016/j.memsci. 2019.03.074
- 37. Aguesse F, López del Amo JM, Roddatis V, Aguadero A, Kilner JA. Enhancement of the grain boundary conductivity in ceramic Li_{0.34}La_{0.55}TiO₃ electrolytes in a moisture-free processing environment. Adv Mater Interfaces. 2014;1(7):1300143. https://doi.org/10.1002/admi.201300143
- 38. Henke BL, Gullikson EM, Davis JC. X-ray interactions: photoabsorption, scattering, transmission, and reflection at E=50-30,000 eV, Z=1-92. At Data Nucl Data Tables. 1993;54(2):181–342. https://doi.org/10.1006/adnd.1993.1013
- Bearden JA. X-ray wavelengths. Rev Mod Phys. 1967;39(1):78–124. https://doi.org/10.1103/RevModPhys.39.78
- Ritchie NWM, Newbury DE, Davis JM. EDS measurements of X-ray intensity at WDS precision and accuracy using a silicon drift detector. Microsc Microanal. 2012;18(4):892–904. https:// doi.org/10.1017/S1431927612001109
- Newbury DE, Ritchie NWM. Performing elemental microanalysis with high accuracy and high precision by scanning electron microscopy/silicon drift detector energy-dispersive X-ray spectrometry (SEM/SDD-EDS). J Mater Sci. 2015;50(2):493–518. https://doi.org/10.1007/s10853-014-8685-2

42. Xu L, Zhang L, Hu Y, Luo L. Structural origin of low Li-ion conductivity in perovskite solid-state electrolyte. Nano Energy. 2022;92:106758. https://doi.org/10.1016/j.nanoen.2021.106758

SUPPORTING INFORMATION

Additional supporting information can be found online in the Supporting Information section at the end of this article. **How to cite this article:** Brummel IA, Wynne K, Lanford WA, Ihlefeld JF. Effects of burial powder configuration on the microstructure, composition, and ion conductivity of perovskite Li_{3x}La_{1/3-x}TaO₃ ion conductors. J Am Ceram Soc. 2022;1–10. https://doi.org/10.1111/jace.18730